Available online at www.sciencedirect.com
SCIENCE DIRECT®
Materials Science and Engineering C 26 (2006) 1232 – 1244
MATERIALS SCIENCE & ENGINEERING C
www.elsevier.com/locate/msec

Molecularly based analysis of deformation of spectrin network and human erythrocyte

M. Dao [a], J. Li [b], S. Suresh [a,c,*]

[a] Department of Materials Science and Engineering, Massachusetts Institute of Technology, Cambridge, MA 02139, USA
[b] Department of Materials Science and Engineering, Ohio State University, Columbus, Ohio 43210, USA
[c] Division of Biological Engineering, Massachusetts Institute of Technology, Cambridge, MA 02139, USA

Available online 26 January 2006

Abstract

We examine the large deformation elastic response of the spectrin network in a human red blood cell (RBC) on the basis of molecular-level constitutive laws. These formulations are shown to be consistent with the predictions of continuum level models for the hyperelastic deformation of RBC, and are compared with recent experimental studies of whole-cell deformation using optical tweezers stretching. Implications of these analysis for extracting cell membrane and cytoskeleton response from whole-cell computational simulations of large deformation for realistic geometries of RBC spectrin network are described. Aspects of large deformation, such as the folding of cell wall during large deformation, are also examined. We also provide general scaling relationships and closed-form functions on the basis of which mechanical properties of RBCs can be extracted from optical tweezers experiments.

Keywords: Red blood cell; Molecular model; Optical tweezers; Spectrin network; Shear modulus; Malaria

1. Introduction

The deformation characteristics of human red blood cells (RBCs) or erythrocytes have been topics of research for decades for a variety of reasons. These non-nucleated cells with their relatively simple subcellular structure devoid of a nucleus and with a nearly two-dimensional spectrin cytoskeleton network offer possibilities to test analytical and computational models on the basis of which more complex analysis can be developed for other complex cells. In addition, the deformation characteristics of the RBCs are known to be strongly linked to the progression and consequences of hereditary hemolytic disorders such as spherocytosis, elliptocytosis and ovalocytosis [1–3], sickle cell disease [4–6] and infectious disease such as malaria (see, for example [7–9], and the references cited therein for more details).

While continuum descriptions of RBC deformation have been the subject of numerous studies [10,11], molecularly based descriptions of spectrin deformation are increasingly being used to address finer-scale and multi-scale mechanical and biochemical coupling (See [12–15] for example, and the references cited therein for more details). Such growing interest in molecularly inspired multi-scale modeling can be attributed to the following recent developments using laser tweezers technique: 1) successful experiments on force-displacement relationships from the stretching of single DNA molecules and proteins (e.g., [16]); 2) large deformation stretching of whole RBCs with picoNewton level force resolution [17,18]; and 3) the ability to determine systematically the mechanical response of the RBC in conjunction with progressive biochemical and substructural changes during events such as controlled parasitization (e.g., [9]). Such molecular level information can also provide potential biochemical pathways to manipulate cytoskeleton deformation. It is, therefore, essential to develop a hierarchical series of multi-scale modeling capabilities that link whole cell deformation (which can be experimentally measured directly) with molecularly based models for subcellular deformation. Advances in computational tools in recent years have provided appealing possibilities to accomplish these goals by incorporating appropriate molecular architecture, defect structure, and multi-scale constitutive formulations for the deformation of whole RBC.

* Corresponding author. Department of Materials Science and Engineering, Massachusetts Institute of Technology, Cambridge, MA 02139, USA.
E-mail address: ssuresh@mit.edu (S. Suresh).

0928-4931/$ - see front matter © 2005 Elsevier B.V. All rights reserved.
doi:10.1016/j.msec.2005.08.020

In this paper, we present formulations whereby different elastic parameters to characterize large deformation of RBCs can be extracted from molecular-level force-displacement relationships. We further show that such formulations are fully consistent with continuum analysis based on hyperelastic constitutive laws and with experimental observations of whole cell deformation. These results are also shown to be consistent with our recent spectrin-level simulations of the entire cell [15]. Aspects of large deformation, such as cell wall folding which have recently been identified on the basis of both continuum [17,18] and molecular-level modeling [14,15], are also examined in the present work.

2. WLC spectrin network membrane model and large deformation elasticity

A healthy erythrocyte or red blood cell (RBC) has a biconcave equilibrium shape with an average size of about 8 μm in long diameter. The RBC transports oxygen from the lungs to the tissues and then transports CO_2 back from the tissues to the lungs via its ~280 million hemoglobin molecules in the cytosol. In this process, the RBC must pass through small capillaries whose inner diameters are smaller than the cell diameter. The cell needs to change from its biconcave shape to a bullet or parachute shape, with maximum in-plane strain on the order of 100% in certain parts of the RBC membrane induced by the local pressure gradient [11]. It is therefore important to understand the RBC membrane within the context of large elastic deformation.

As illustrated in Fig. 1(a), the RBC cell wall comprises a phospholipid bilayer, cholesterol molecules, transmembrane proteins and an underlying spectrin network which is tethered to the membrane. These structural components collectively determine the deformation behavior of the RBC, in addition to performing their normal biological functions. The basic building block of the load-bearing RBC cytoskeleton structure is the spectrin heterodimer, consisting of intertwined α (280 kD) and β (246 kD) polypeptide chains running antiparallel to one other [19]. By using the worm-like-chain (WLC) model to describe the nonlinear force-displacement behavior of each individual spectrin molecule (Fig. 1(b)) [13,15], the large deformation characteristics of the RBC membrane can be obtained in terms of the persistent length, p, the equilibrium length L_0, and the maximum extension length, L_{max}, of the spectrin link. The effective membrane behavior can also be described phenomenologically using continuum hyperelasticity models [10,17] where the membrane mechanical properties are represented by shear modulus, μ, and bending stiffness, κ (Fig. 1(c)).

2.1. Spectrin network model

In our recent work [15], a spectrin network model was constructed to analyze the large deformation of the erythrocyte, extending the earlier work of Discher and coworkers [13,20–22]. The approach in [15] particularly focused on incorporating the effects of random spectrin network, structural relaxation of the in-plane shear energy, and to include the spontaneous curvature of the lipid bilayers material [23–25].

The degrees of freedom of the model are the actin vertex coordinates $\{\boldsymbol{x}_n\}$, $n \in 1..N$, which can move freely in 3D Cartesian space according to the generalized force on each vertex. This is schematically illustrated in Fig. 2(a). Between a vertex pair (m, n), there can be a spectrin link $i \in 1..S$ whose length is $L_i \equiv |\boldsymbol{x}_m - \boldsymbol{x}_n|$, the assembly of which forms a 2-D network. A vertex triplet (l, m, n), mutually connected by spectrin molecules, forms a triangle $\alpha \in 1..\Pi$, whose area is

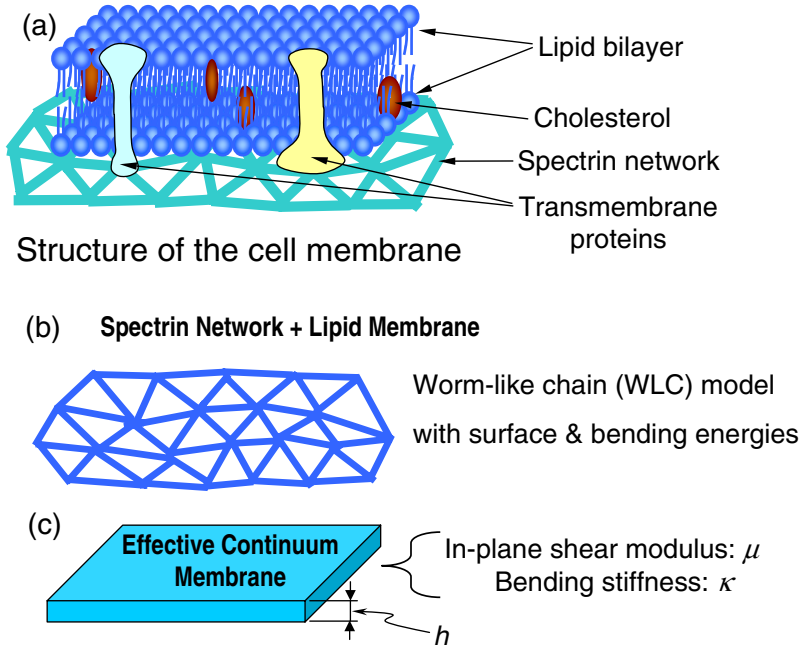

Fig. 1. Molecular based and continuum models of RBC membrane. (a) schematic drawing of the RBC membrane structure (not to scale). (b) molecular based model. (c) effective continuum membrane.

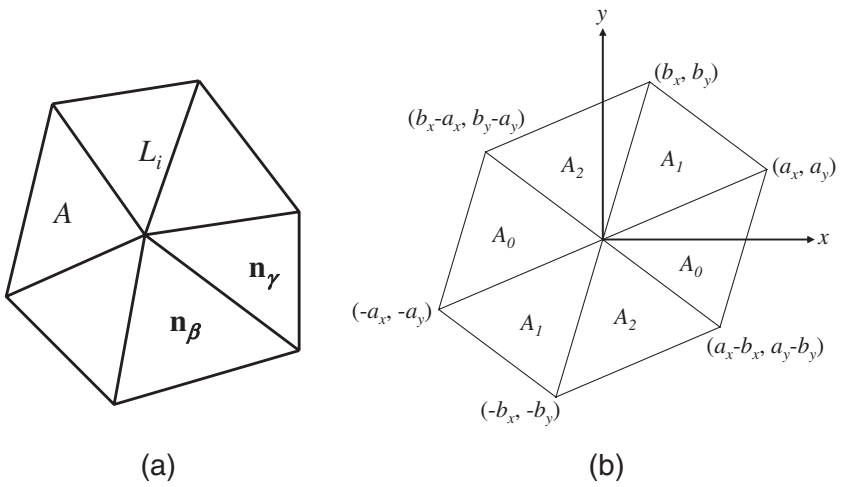

Fig. 2. Schematic drawings of the WLC-membrane model. (a) a degree 6 triangle dominated cytoskeleton model. L_i marks a link between two adjacent junction complexes, which is characterized by the WLC force-extension relationship. A_α is the area of a triangular plaquette, and n_β and n_γ are the normal vectors to plaquette β and γ, respectively. (b) A regular "single crystal" cytoskeleton network.

$A_\alpha = |(\boldsymbol{x}_m - \boldsymbol{x}_l) \times (\boldsymbol{x}_n - \boldsymbol{x}_l)|/2$ and center of mass is $\boldsymbol{x}_\alpha \equiv (\boldsymbol{x}_l + \boldsymbol{x}_m + \boldsymbol{x}_n)/3$, and whose normal $\mathbf{n}_\alpha$ points towards cell exterior. Two triangles α and β are considered to be adjacent if they share a common spectrin link. The total coarse-grained Helmholtz free energy of such a RBC cytoskeleton system is [13,15]:

$$F(\{x_n\}) = F_{\text{in-plane}} + F_{\text{bending}} + F_{\text{surface constraint}} + F_{\text{volume constraint}} \quad (1)$$

Noting that in the context of large deformation studies such as optical tweezers experiments, $F_{\text{in-plane}}$ is the dominant active term in Eq. (1). The spectrin network plus the bilayer membrane is assumed to have a total free energy [15]

$$F_{\text{in-plane}} = \sum_{i \in \text{ spectrin links}} V_{\text{WLC}}(L_i) + \sum_{\alpha \in \text{triangular plaquettes}} \frac{C_q}{A_\alpha^q} \quad (2)$$

where L_i is the length of spectrin link i and A_α is the area of triangular plaquette α. The first summation in Eq. (2) includes all spectrin links and is the total entropic free energy stored in the spectrin proteins described in terms of the WLC model [16,26], where the force versus chain length relationship is:

$$f_{\text{WLC}}(L) = -\frac{k_B T}{p}\left\{\frac{1}{4(1-x)^2} - \frac{1}{4} + x\right\},$$
$$x \equiv \frac{L}{L_{\max}} \in [0, 1), \quad (3)$$

in which $L_{\max}$ is the maximum or contour length of the chain, L is the instantaneous chain length (x is the dimensionless ratio between L and $L_{\max}$), p is the persistence length, k_B is the Boltzmann constant, and T is the temperature. Integrating Eq. (3) gives the result [13] that

$$V_{\text{WLC}}(L) = -\int_0^L d\xi f_{\text{WLC}}(\xi) = \frac{k_B T L_{\max}}{4p} \cdot \frac{3x^2 - 2x^3}{1-x}. \quad (4)$$

The second summation in Eq. (2) is the hydrostatic elastic energy stored in the lipid membrane and other protein molecules, with constant C_q and exponent q to be selected. Here we use $q=1$ in this study. The second, third and fourth free energy terms in Eq. (1) were defined similarly as traditional cell elasticity models, where detailed developments can be found elsewhere [15].

2.2. Large deformation elasticity constitutive equations of WLC membrane

Suppose that the spectrin network is a 2-D triangular crystal (Fig. 2(b)) with Bravais lattice vectors $\boldsymbol{a} \equiv (a_x, a_y)$ and $\boldsymbol{b} \equiv (b_x, b_y)$. The parameter set $\{a_x, a_y, b_x, b_y\}$ determines completely the geometry of the membrane cytoskeleton. For a given reference lattice, $\{a_x, a_y, b_x, b_y\}$ can be made equivalent to two diagonal and one off-diagonal strain and one rotational degree of freedom. Then,

$$\boldsymbol{c} \equiv \boldsymbol{b} - \boldsymbol{a} = (b_x - a_x, b_y - a_y), \quad (5)$$

$$a \equiv |\boldsymbol{a}| = \sqrt{a_x^2 + a_y^2},\ b \equiv |\boldsymbol{b}| = \sqrt{b_x^2 + b_y^2},$$
$$c \equiv |\boldsymbol{c}| = \sqrt{(b_x - a_x)^2 + (b_y - a_y)^2}. \quad (6)$$

All triangles in the perfect crystalline arrangement have the same area:

$$A_0 = A_1 = A_2 = A = \frac{1}{2}|\boldsymbol{a} \times \boldsymbol{b}| = \frac{1}{2}|a_x b_y - a_y b_x|. \quad (7)$$

If a right-handed system is always chosen, that is, if $\boldsymbol{b}$ is always chosen to be counter-clockwise to $\boldsymbol{a}$, then the above symbols || for absolute values in Eqs. (6) and (7) can be dropped.

The next step is to perform a nonlinear elasticity analysis for the given Bravais lattice $\{\boldsymbol{a}, \boldsymbol{b}\}$. Each vertex is connected to 6 spectrin links, but each link is shared by two vertices, such that each vertex has three links associated with it. These three links are conveniently chosen to be $\boldsymbol{a}$, $\boldsymbol{b}$, $\boldsymbol{c}$, respectively, with the associated WLC energy being $V_{\text{WLC}}(a) + V_{\text{WLC}}(b) + V_{\text{WLC}}(c)$. Similarly, each vertex is connected to 6 triangular plaquettes, but a triangular plaquette is shared by 3 vertices. Thus each vertex really has two affiliated plaquettes, with associated

membrane energy being $2\times C_q A^{-q}$. So for each vertex that occupies a current area $2A$ the associated strain energy is $V_{\mathrm{WLC}}(a)+V_{\mathrm{WLC}}(b)+V_{\mathrm{WLC}}(c)+2C_qA^{-q}$. Based on the Virial theorem [27], the Cauchy stress is:

$$\tau_{\alpha\beta} = -\frac{1}{S}\sum_{r_k\in\mathrm{pair}} r_k f(r_k)\hat{r}_k^{\alpha}\hat{r}_k^{\beta} = -\frac{1}{S}\sum_{r_k\in\mathrm{pair}} \frac{f(r_k)}{r_k} r_k^{\alpha} r_k^{\beta} \tag{8}$$

for pair-interactions, where S is the area of the representative area element (RAE), and k goes over all interacting pairs in the RAE, each pair with radial distance r_k, directional normal $\hat{\mathbf{r}}_k$ and interacting force $f(r_k)\hat{\mathbf{r}}_k$. The corresponding WLC stress then is derived to be:

$$\tau_{\alpha\beta}^{\mathrm{WLC}} = -\frac{1}{2A}\left[\frac{f_{\mathrm{WLC}}(a)}{a}a_\alpha a_\beta + \frac{f_{\mathrm{WLC}}(b)}{b}b_\alpha b_\beta + \frac{f_{\mathrm{WLC}}(c)}{c}c_\alpha c_\beta\right]. \tag{9}$$

The membrane term, on the other hand, creates a purely hydrostatic stress contribution,

$$\tau_{\alpha\beta}^{\mathrm{membrane}} = -\frac{1}{2}\left[2qC_qA^{-q-1}\right]\delta_{\alpha\beta} = -qC_qA^{-q-1}\delta_{\alpha\beta}. \tag{10}$$

The total in-plane stress is simply the summation of (9) and (10):

$$\tau_{\alpha\beta} = -\frac{1}{2A}\left[\frac{f_{\mathrm{WLC}}(a)}{a}a_\alpha a_\beta + \frac{f_{\mathrm{WLC}}(b)}{b}b_\alpha b_\beta + \frac{f_{\mathrm{WLC}}(c)}{c}c_\alpha c_\beta\right] - qC_qA^{-q-1}\delta_{\alpha\beta}. \tag{11}$$

Now suppose that at $a=b=c=L_0=x_0L_{\max}$ in an undeformed lattice, $\tau_{\alpha\beta}=0$. Then,

$$\begin{aligned} 0 &= \frac{1}{2A_0L_{\max}x_0}\cdot -\frac{k_BT}{p}\left\{\frac{1}{4(1-x_0)^2}-\frac{1}{4}+x_0\right\} \\ &\quad\times\left[a_\alpha a_\beta + b_\alpha b_\beta + c_\alpha c_\beta\right] + qC_qA_0^{-q-1}\delta_{\alpha\beta} \\ &= \frac{1}{2A_0L_{\max}x_0}\cdot -\frac{k_BT}{p}\left\{\frac{1}{4(1-x_0)^2}-\frac{1}{4}+x_0\right\} \\ &\quad\times\left[(x_0L_{\max})^2\frac{3\delta_{\alpha\beta}}{2}\right] + qC_qA_0^{-q-1}\delta_{\alpha\beta} \end{aligned} \tag{12}$$

with $A_0=\sqrt{3}(x_0L_{\max})^2/4$. Consequently,

$$\begin{aligned} C_q &= \frac{3A_0^q}{4qL_{\max}x_0}\cdot\frac{k_BT}{p}\left\{\frac{1}{4(1-x_0)^2}-\frac{1}{4}+x_0\right\}(x_0L_{\max})^2 \\ &= \frac{3A_0^qL_{\max}x_0^2k_BT(6-9x_0+4x_0^2)}{16pq(1-x_0)^2}. \end{aligned} \tag{13}$$

In the special case of $q=1$ [13],

$$C_1 = \frac{3\sqrt{3}L_{\max}^3x_0^4k_BT(6-9x_0+4x_0^2)}{64p(1-x_0)^2}. \tag{14}$$

2.3. Comparison of WLC spectrin network model and hyperelasticity model

Following the classical rubber elasticity formulations (see, for example [28,29]), we have applied first order neo-Hookean as well as third order hyperelasticity model to study RBC deformation [17,18]. Expressing the strain energy potential in terms of membrane shear modulus (in units of force per unit length),

$$\Phi = \frac{\mu_0}{2}\left(\lambda_1^2+\lambda_2^2+\lambda_3^2-3\right)+\mu_{\mathrm{h}}\left(\lambda_1^2+\lambda_2^2+\lambda_3^2-3\right)^3, \tag{15}$$

where μ_0 is the initial membrane shear modulus (in units of force per unit length), μ_{h} is the third order hyperelasticity constant, and λ_{i} ($i=1, 2, 3$) are the principal stretches. If the membrane is assumed to be incompressible, $\lambda_1\lambda_2\lambda_3=1$. The μ_0/μ_{h} ratio for healthy RBCs as well as malaria parasite infected RBCs were estimated to be around 1/20 to 1/30; and the average initial shear modulus μ_0 for healthy RBCs was estimated to be 5–8 μN/m [9,18], which is consistent with 4–9 μN/m reported in the literature using micropipette experiments [24].

When taking $\mu_{\mathrm{h}}=0$, Eq. (15) describes the neo-Hookean model. When $\mu_{\mathrm{h}}=0$ and $\lambda_1\lambda_2=\lambda_3=1$ (i.e., area conservation), Eq. (15) is reduced to the classical RBC membrane model [10]:

$$T_s = 2\mu_0\gamma = \frac{\mu_0}{2}\left(\lambda_1^2-\lambda_2^2\right), \tag{16a}$$

$$T_s = \frac{1}{2}(T_1-T_2)$$

and

$$\gamma \equiv \frac{1}{2}(\varepsilon_1-\varepsilon_2) = \frac{1}{4}\left(\lambda_1^2-\lambda_2^2\right), \tag{16b}$$

$$\lambda_1\lambda_2 = 1 \tag{16c}$$

where T_1 and T_2 are the in-plane principal membrane stresses, ε_1 and ε_2 are the in-plane principal Green's strains of the membrane, and γ is the shear strain. Noting that, under uniaxial stretching, with the same initial uniaxial response $\frac{\partial T_1}{\partial\lambda_1}|_{\lambda=1}$, the shear modulus μ_0 extracted with or without the area conservation assumption is slightly different. The μ_0 extracted with the area conservation condition enforced ($\lambda_1\lambda_2=1$) would be exactly 75% of that extracted without enforcing this condition. This result is confirmed by the numerical simulations in this study and in a previous study [18]. For example, with the same whole cell stretching response, the extracted shear modulus μ_0 is 5.5 μN/m with area conservation condition enforced, and 7.3 μN/m without enforcing this condition [18]. It is generally accepted in the literature that the RBC membrane can be treated as area conserving, although when severely stretched it can be expanded up to 7% [11].

Consider a reference lattice in equilibrium in Fig. 2(b) with the coordinates

$$\boldsymbol{a}_0 = x_0L_{\max}\left(\frac{\sqrt{3}}{2},\frac{1}{2}\right),\ \boldsymbol{b}_0 = x_0L_{\max}(0,1),$$

$$\boldsymbol{c}_0 = x_0L_{\max}\left(-\frac{\sqrt{3}}{2},\frac{1}{2}\right). \tag{17}$$

Fig. 3 compares the uniaxial stress–strain behavior of the WLC spectrin network model and the hyperelasticity model; the solid curves are computed using the estimated hyperelasticity parameters [18] and the dotted curves are plotted using the estimated WLC parameters [15]. Reasonable match to the initial shear modulus μ_0 as well as the strain hardening behavior of the experimentally estimated hyperelastic response can be found by slightly adjusting the

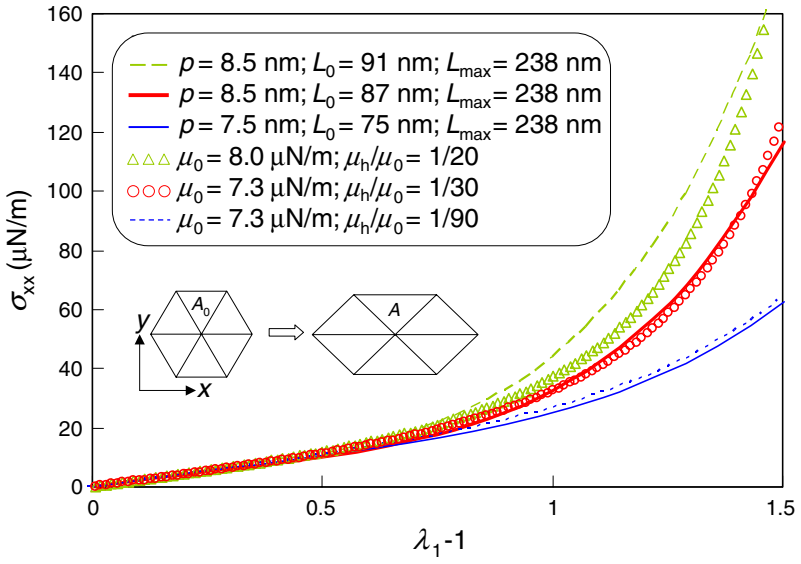

Fig. 3. WLC-membrane uniaxial response versus hyperelasticity model.

parameters p and L_0. This also demonstrates that the microscopic mechanical response is sensitive to microstructural changes.

2.4. Membrane shear modulus μ_0 of the WLC sheet

Again taking the reference configuration as described in Eq. (17), if an incremental engineering shear strain γ is imposed on this lattice,

$$\boldsymbol{J}=\begin{pmatrix}1 & \gamma/2\\ \gamma/2 & 1\end{pmatrix},\ \boldsymbol{r}'=\boldsymbol{r}\boldsymbol{J},\ \Delta|\boldsymbol{r}|\equiv|\boldsymbol{r}'|-|\boldsymbol{r}|=|\boldsymbol{r}|\gamma\hat{r}_x\hat{r}_y+O(\gamma^2), \tag{18}$$

then,

$$\begin{aligned}
&\boldsymbol{a}=x_0L_{\max}\left(\frac{\sqrt{3}}{2}+\frac{\gamma}{4},\frac{1}{2}+\frac{\sqrt{3}\gamma}{4}\right),\\
&\Delta a=x_0L_{\max}\frac{\sqrt{3}\gamma}{4}+O(\gamma^2),\\
&\boldsymbol{b}=x_0L_{\max}\left(\frac{\gamma}{2},\ 1\right),\ \Delta b=O(\gamma^2),\\
&\boldsymbol{c}=x_0L_{\max}\left(-\frac{\sqrt{3}}{2}+\frac{\gamma}{4},\frac{1}{2}-\frac{\sqrt{3}\gamma}{4}\right),\\
&\Delta c=-x_0L_{\max}\frac{\sqrt{3}\gamma}{4}+O(\gamma^2)
\end{aligned} \tag{19}$$

and

$$\Delta A\equiv(\det\boldsymbol{J}-1)A_0=O(\gamma^2), \tag{20}$$

Taking the differential of Eq. (11),

$$\begin{aligned}
\Delta\tau_{xy}=&-\frac{1}{2A_0}\left[\Delta\left(\frac{f_{\mathrm{WLC}}(a)}{a}\right)(a_xa_y)_0+\frac{f_{\mathrm{WLC}}(a_0)}{a_0}\Delta(a_xa_y)\right.\\
&+\frac{f_{\mathrm{WLC}}(b_0)}{b_0}\Delta(b_xb_y)+\Delta\left(\frac{f_{\mathrm{WLC}}(c)}{c}\right)(c_xc_y)_0\\
&\left.+\frac{f_{\mathrm{WLC}}(c_0)}{c_0}\Delta(c_xc_y)\right]+O(\gamma^2).
\end{aligned} \tag{21}$$

With the WLC force-displacement response,

$$\begin{aligned}
\frac{f_{\mathrm{WLC}}(a_0)}{a_0}&=\frac{f_{\mathrm{WLC}}(b_0)}{b_0}=\frac{f_{\mathrm{WLC}}(c_0)}{c_0}\\
&=-\frac{k_BT}{px_0L_{\max}}\left\{\frac{1}{4(1-x_0)^2}-\frac{1}{4}+x_0\right\},
\end{aligned} \tag{22}$$

$$\begin{aligned}
&\Delta(a_xa_y)=\frac{\gamma}{2}(x_0L_{\max})^2,\ \Delta(b_xb_y)=\frac{\gamma}{2}(x_0L_{\max})^2,\\
&\Delta(c_xc_y)=\frac{\gamma}{2}(x_0L_{\max})^2,
\end{aligned} \tag{23}$$

$$\begin{aligned}
&\frac{f_{\mathrm{WLC}}(a_0)}{a_0}\Delta(a_xa_y)+\frac{f_{\mathrm{WLC}}(b_0)}{b_0}\Delta(b_xb_y)+\frac{f_{\mathrm{WLC}}(c_0)}{c_0}\Delta(c_xc_y)\\
&=-\frac{3\gamma k_BTx_0L_{\max}}{2p}\left\{\frac{1}{4(1-x_0)^2}-\frac{1}{4}+x_0\right\}.
\end{aligned} \tag{24}$$

On the other hand,

$$(a_xa_y)_0=(x_0L_{\max})^2\frac{\sqrt{3}}{4},\ (c_xc_y)_0=-(x_0L_{\max})^2\frac{\sqrt{3}}{4}, \tag{25}$$

and,

$$\frac{f_{\mathrm{WLC}}(L)}{L}=-\frac{k_BT}{pL}\left\{\frac{1}{4(1-x)^2}-\frac{1}{4}+x\right\}, \tag{26}$$

so,

$$\begin{aligned}
\Delta\frac{f_{\mathrm{WLC}}(L)}{L}&=\frac{k_BT}{pL_0^2}\left\{\frac{1}{4(1-x_0)^2}-\frac{1}{4}+x_0\right\}\Delta L-\frac{k_BT}{pL_0}\\
&\quad\times\left\{\frac{1}{2(1-x_0)^3}+1\right\}\frac{\Delta L}{L_{\max}}\\
&=\frac{k_BT}{pL_0^2}\left\{\frac{1}{4(1-x_0)^2}-\frac{x_0}{2(1-x_0)^3}-\frac{1}{4}\right\}\Delta L.
\end{aligned} \tag{27}$$

Thus,

$$\Delta\left(\frac{f_{\mathrm{WLC}}(a)}{a}\right)(a_x a_y)_0+\Delta\left(\frac{f_{\mathrm{WLC}}(c)}{c}\right)(c_x c_y)_0 = \frac{3\gamma k_B T x_0 L_{\max}}{8p}\left\{\frac{1}{4(1-x_0)^2}-\frac{x_0}{2(1-x_0)^3}-\frac{1}{4}\right\}. \quad (28)$$

Combining contributions in Eqs. (27) and (28), it is seen that

$$\mu_0 \equiv \frac{d\tau_{xy}}{d\gamma} = \frac{1}{2A_0}\frac{3k_B T x_0 L_{\max}}{8p}\left\{\frac{1}{(1-x_0)^2}-1+4x_0 - \frac{1}{4(1-x_0)^2}+\frac{x_0}{2(1-x_0)^3}+\frac{1}{4}\right\} = \frac{\sqrt{3}k_B T}{4pL_{\max}x_0}\left\{\frac{3}{4(1-x_0)^2}-\frac{3}{4}+4x_0+\frac{x_0}{2(1-x_0)^3}\right\}. \quad (29)$$

This equation provides an explicit expression for the shear modulus of the cell membrane which is envisioned as comprising a triangulated network of WLC spectrin molecules anchored at actin vertices.

If we take $p=8.5$ nm, $L_0=87$ nm, and $L_{\max}=238$ nm, Eq. (29) gives linear shear modulus $\mu_0=7.98$ μN/m. This has been verified numerically by studying the behavior of the implementation of the large-strain formula Eq. (11) at small strain. In particular, we select two area-preserving deformation paths,

$$\mathbf{J}_1(\gamma)=\begin{pmatrix}1 & 0\\ \gamma & 1\end{pmatrix}, \quad \mathbf{J}_2(\gamma)=\begin{pmatrix}1 & \gamma\\ 0 & 1\end{pmatrix}, \quad (30)$$

and plot σ_{xy} versus γ in Fig. 4. The two paths have the same linear shear modulus μ_0 at small γ but the behaviors diverge at large γ, as one path causes shear displacement in the x-direction, and the other in the y-direction. This illustrates that the "single-crystal" WLC membrane is isotropic linear elastically, but anisotropic at large deformation. The non-textured "polycrystalline" or "amorphous" versions of the WLC membrane should be isotropic even for large deformation.

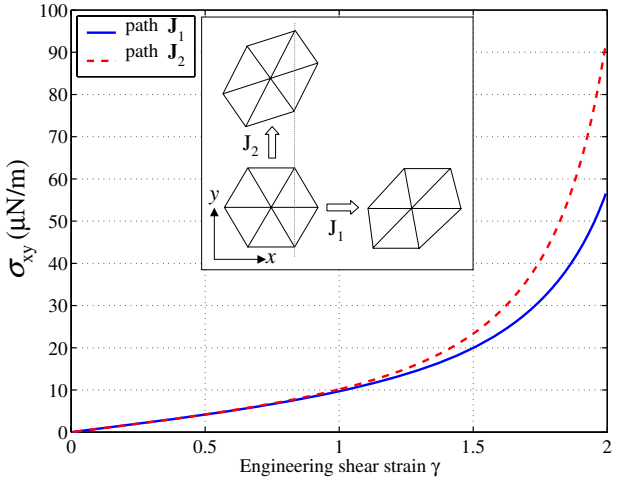

Fig. 4. Large-strain response of "single-crystal" WLC membrane ($p=8.5$ nm, $L_0=87$ nm, $L_{\max}=238$ nm) for two area-preserving shear paths $\mathbf{J}_1$ and $\mathbf{J}_2$ shown in Eq. (30).

2.5. Linear elastic area compression modulus K of the WLC sheet

When $a=b=c=L_{\max}x$ and the angle between $\boldsymbol{a},\boldsymbol{b}$ is exactly 60°, the Cauchy stress is diagonal:

$$\tau_{\alpha\beta}=\frac{1}{2A}\cdot\frac{k_B T}{pL_{\max}x}\left\{\frac{1}{4(1-x)^2}-\frac{1}{4}+x\right\}\left[(xL_{\max})^2\frac{3\delta_{\alpha\beta}}{2}\right] - qC_q A^{-q-1}\delta_{\alpha\beta}. \quad (31)$$

The resulting pressure is

$$P=qC_q A^{-q-1}-\frac{3k_B T x L_{\max}}{4Ap}\left\{\frac{1}{4(1-x)^2}-\frac{1}{4}+x\right\}. \quad (32)$$

The linear elastic area compression modulus K is defined as,

$$K\equiv -\left.\frac{\partial P}{\partial \log A}\right|_{A=A_0} = -\frac{1}{2}\left.\frac{\partial P}{\partial \log x}\right|_{x=x_0}. \quad (33)$$

With the definition,

$$U\equiv qC_q A^{-q-1}, V\equiv\frac{3k_B T x L_{\max}}{4Ap}\left\{\frac{1}{4(1-x)^2}-\frac{1}{4}+x\right\},$$

$$P=U-V, U_0\equiv U(x_0)=V_0\equiv V(x_0)=qC_q A_0^{-q-1}. \quad (34)$$

It is seen that

$$\left.\frac{\partial U}{\partial \log x}\right|_{x=x_0}=U_0\left.\frac{\partial \log U}{\partial \log x}\right|_{x=x_0} U_0(-q-1)\times 2, \quad (35)$$

and that,

$$\left.\frac{\partial V}{\partial \log x}\right|_{x=x_0}=V_0\left.\frac{\partial \log V}{\partial \log x}\right|_{x=x_0} = U_0\left\{-1+\frac{2+4(1-x_0)^3}{(1-x_0)(6-9x_0+4x_0^2)}\right\}. \quad (36)$$

Thus,

$$K=-\frac{1}{2}\left(\left.\frac{\partial U}{\partial \log x}\right|_{x=x_0}-\left.\frac{\partial V}{\partial \log x}\right|_{x=x_0}\right) = qC_q A_0^{-q-1}\left\{q+\frac{1}{2}+\frac{1+2(1-x_0)^3}{(1-x_0)(6-9x_0+4x_0^2)}\right\}. \quad (37)$$

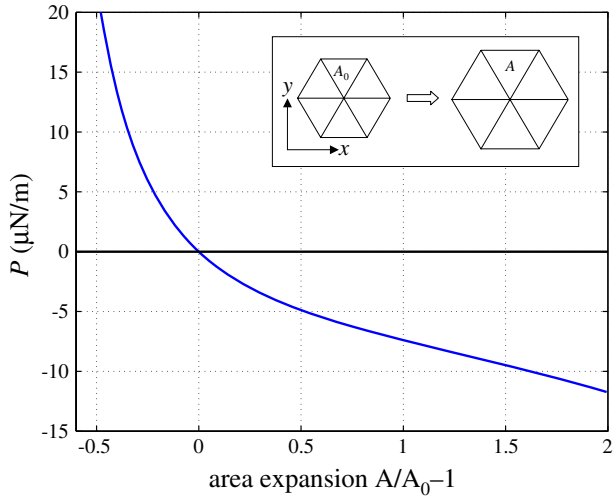

Fig. 5. Large-strain response of "single-crystal" WLC membrane (p=8.5 nm, L_0=87 nm, L_{max}=238 nm) under area expansion and compression.

Combining this expression with Eq. (13),

$$K = \frac{3L_{\max}x_0^2 k_B T\left(6-9x_0+4x_0^2\right)}{16p(1-x_0)^2 A_0} \times \left\{q+\frac{1}{2}+\frac{1+2(1-x_0)^3}{(1-x_0)\left(6-9x_0+4x_0^2\right)}\right\} = \frac{\sqrt{3}k_B T}{4pL_{\max}(1-x_0)^2}\left\{\left(q+\frac{1}{2}\right)\left(6-9x_0+4x_0^2\right) + \frac{1+2(1-x_0)^3}{1-x_0}\right\}. \quad (38)$$

For p=8.5 nm, L_0=87 nm, and L_{max}=238 nm, Eq. (38) gives linear shear modulus K=15.96 μN/m. The behavior at large strain is shown in Fig. 5.

2.6. Linear elastic Young's modulus E and Poisson's ratio ν of the WLC Sheet

For small deformations, the sheet is an isotropic elastic medium, with

$$C_{ijkl} = \lambda\delta_{ij}\delta_{kl} + \mu_0\left(\delta_{ik}\delta_{jl}+\delta_{il}\delta_{jk}\right), \quad i,j,k,l,\in 1,2, \quad (39)$$

which complies with all symmetry requirements and tensor-transformation law:

$$Q_{ii'}Q_{jj'}Q_{kk'}Q_{ll'}C_{ijkl} = C_{i'j'k'l'}. \quad (40)$$

In matrix notation,

$$\mathbf{C} = \begin{pmatrix} \lambda+2\mu_0 & \lambda & 0 \\ \lambda & \lambda+2\mu_0 & 0 \\ 0 & 0 & \mu_0 \end{pmatrix}. \quad (41)$$

Note that $K=\lambda+\mu_0$, or $\lambda=K-\mu_0$, such that

$$\begin{pmatrix} \lambda+2\mu_0 & \lambda \\ \lambda & \lambda+2\mu_0 \end{pmatrix}\begin{pmatrix} 1 \\ -\frac{\lambda}{\lambda+2\mu_0} \end{pmatrix} = \begin{pmatrix} \lambda+2\mu_0-\frac{\lambda^2}{\lambda+2\mu_0} \\ 0 \end{pmatrix}. \quad (42)$$

The linear elastic Young's modulus is therefore:

$$E = \lambda+2\mu_0-\frac{\lambda^2}{\lambda+2\mu_0} = \frac{4\mu_0^2+4\lambda\mu_0}{\lambda+2\mu_0} = \frac{4K\mu_0}{K+\mu_0}, \quad (43)$$

and the Poisson's ratio is:

$$\nu = \frac{\lambda}{\lambda+2\mu_0} = \frac{K-\mu_0}{K+\mu_0} \quad (44)$$

Unlike pair-potential systems [30], ν in general is not 1/3. However, if q=1, then ν happens to be 1/3. One may directly verify that Eq. (38) is exactly twice of Eq. (29) when q=1. This result is consistent with a recent measurement, where K/μ_0 was found to be 1.9 [31].

3. Modeling whole cell deformation of the erythrocyte

3.1. Molecularly based and continuum whole cell model setup

Experimental techniques of laser or optical tweezers (also referred to as laser or optical traps) were used in measuring mechanical response of living cells with maximum force resolution on the order of 1 pN [32]. Systematic experiments on healthy RBCs [18] as well as RBCs invaded by the malaria parasite, *Plasmodium falciparum* [9] were performed with maximum loading forces on the order of 200 pN, which is capable of stretching the RBC axial diameter to twice of its original diameter. Corresponding spectrin network model [15] and continuum finite element model [17] were constructed to study the whole cell deformation under laser tweezers stretching.

Fig. 6 schematically illustrates the experimental setup of laser tweezers as well as the molecularly based and continuum finite element computational model setup. In the laser tweezers experiment [18], silica beads 4.12 μm in diameter (Bangs Laboratories, Fisher, IN, U.S.A.) were added to RBCs to introduce spontaneous and nonspecific bonding. The optical tweezers system incorporates a 1.5 W, 1064 nm Nd:YAG laser module (LazerTweezers, Cell Robotics, Inc., Albuquerque, NM, U.S.A.) and inverted optical microscope (Leica Systems, Wetslar, Germany). Deformation was captured using a CCD camera whereby real-time video images can be viewed. Detailed descriptions of cell and bead preparation for stretching healthy and parasitized RBCs by optical tweezers and of the calibration methods can be found elsewhere [18]. This experimental setup can be used to measure the deformed axial diameter, D_A, and the deformed transverse diameter, D_T, versus the total stretching force, F. The initial cell size, D_0, and the contact diameter, d_c (taken to be the average value from the two diametrically contacting beads), are measured experimentally (see Fig. 6).

In setting up the molecularly based and the continuum whole cell model under laser tweezers stretching, the starting cell geometry is taken to be the average geometry of healthy RBCs given by [33],

$$z = \pm D_0\sqrt{1-\frac{4(x^2+y^2)}{D_0^2}}\left[c_0+c_1\frac{x^2+y^2}{D_0^2}+c_2\frac{(x^2+y^2)^2}{D_0^4}\right] \quad (45)$$

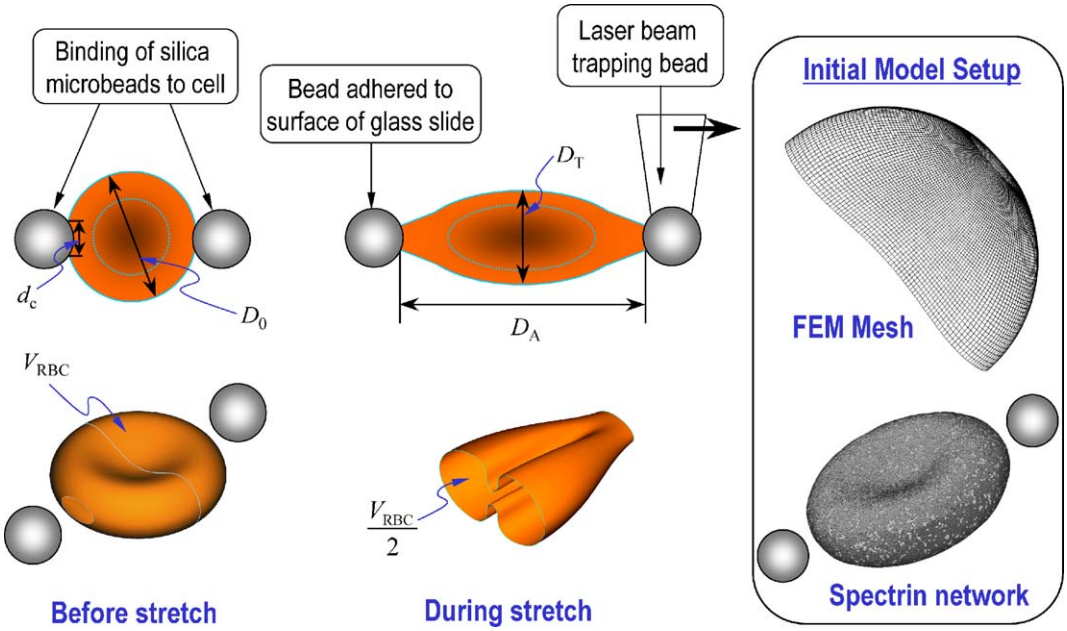

Fig. 6. Laser tweezers experiment and computational models setup.

where the parameter set $(D_0, c_0, c_1, c_2)=(7.82\ \mu m, 0.05179025, 2.002558, -4.491048)$ describes the biconcave shape of an average healthy RBC, with the cytosol volume $V_{RBC}=94\ \mu m^3$ and the cell surface area $A_{RBC}=135\ \mu m^2$. The parameter set $(D_0, c_0, c_1, c_2)=(6.54\ \mu m, 0.5, 0, 0)$ describes the spherical shape with the same surface area A_{RBC}, where the biconcave shape can be achieved via a sophisticated random network generation and morphing process [15]. The relaxed, free-standing, biconcave shape so achieved with the WLC spectrin network model consists of $N=28{,}673$ vertices (see Fig. 7), which is only slightly deviated from the above mentioned analytical biconcave shape. This spectrin network is dominated by degree-6 connectivity (i.e., a node connected with 6 spectrin links), and each connected spectrin link is described by the WLC force-displacement law given by Eq. (3). The biconcave-shaped WLC spectrin network model so generated has zero initial in-plane deformation energy and a small bending energy on the order of 10–100 eV, which does not have any significant influences towards the subsequent laser tweezers stretching response. The total cytosol volume, V_{RBC}, and the membrane surface area, A_{RBC}, are constrained to be fairly close to their initial values, respectively. The detailed model generation process of the WLC spectrin network can be found in [15].

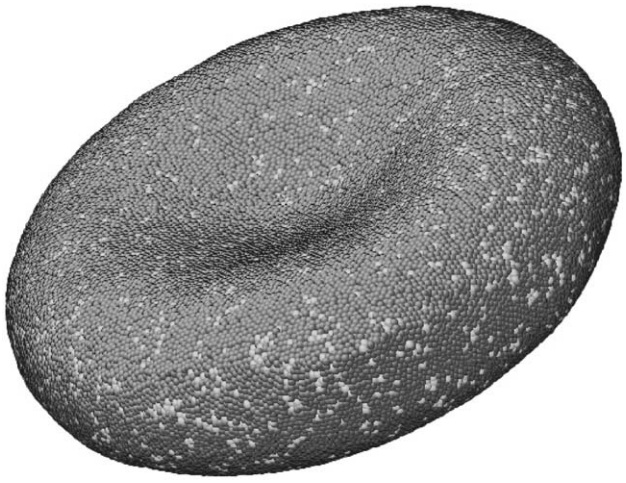

Fig. 7. WLC spectrin network RBC model setup.

In the molecularly based model simulations, a time-dependent total force $F^{ext}(t)$ is applied to $N_+=0.05N$ vertices of the cytoskeleton in the x-direction, which are chosen to be 5% of vertices that have the largest x-coordinates at the beginning of the simulation. Correspondingly, a $-F^{ext}(t)$ total force is applied to $N_-=0.05N$ vertices that have the smallest x-coordinates at the beginning of the simulation. Thus, $f_n^{ext}=\pm F^{ext}(t)/(0.05N)$ if vertex n is in N_+/N_-, and 0 if otherwise. The choice of $0.05N$ vertices corresponds to a contact diameter $d_c\approx 2\ \mu m$. The contact diameter d_c can be easily adjusted by changing the percentage of N vertices which $\pm F^{ext}(t)$ is applied to.

In the continuum finite element simulations, the stress-free configuration is taken to be the analytical biconcave shape described above. The stretching force is applied to the silica microbeads which are attached diametrically at opposite ends of the cell. The silica beads are modeled as rigid spheres and are assumed to be attached to the cell over a small oval region with a diameter of between 0.5 to 2 μm so that the contact diameter can be simulated in accordance with the experimentally observed values. To simulate laser tweezers experiments, only half of the red blood cell is modeled due to symmetry with 12,000 three-dimensional shell elements (see inset in Fig. 6). Four-noded, bilinear, reduced integration shell elements are used. Full cell simulations are also performed to study shape evolution versus membrane shear and bending moduli. The total cytosol volume, V_{RBC}, is kept constant at the initial value

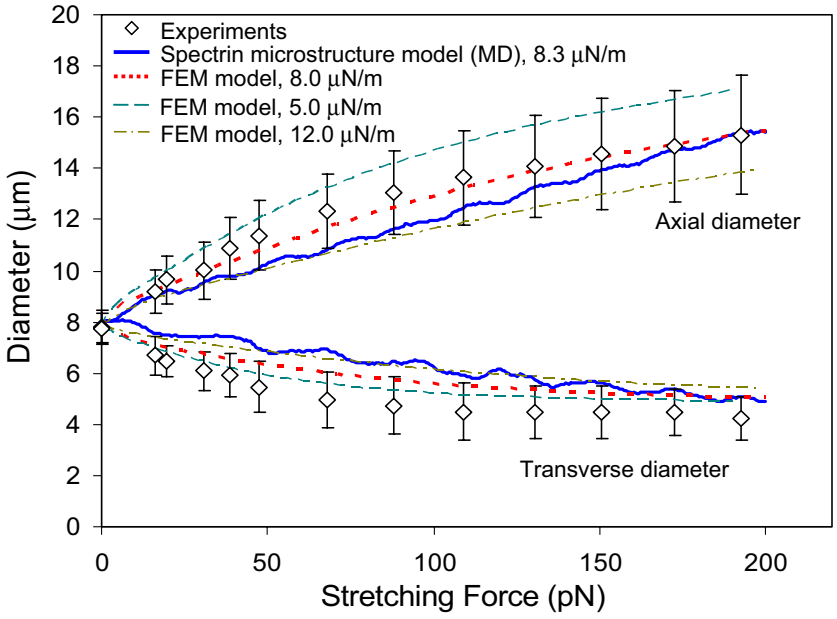

Fig. 8. Computational results using molecular based and continuum model versus experimental data.

throughout the simulations. The simulations have been performed using the commercially available general purpose finite element package, ABAQUS (ABAQUS Inc., Pawtucket, RI, U.S.A.).

3.2. Laser tweezers simulation results

The coarse grained molecular dynamics (CGMD) simulation is carried out using the following parameter set: $L_0=75$ nm, $L_{max}=3.17L_0=238$ nm, $p=0.1L_0=7.5$ nm, $q=1$, and additional terms related to volume and surface area conservation and bending energy. This parameter set leads to the following linear elastic properties for the molecularly based WLC sheet: shear modulus $\mu_0=8.3$ μN/m; area dilatational modulus $K=16.6$ μN/m; uniaxial tension Young's modulus $E=22.1$ μN/m; Poisson's ratio $\nu=1/3$; and average bending modulus $\kappa=2.4\times10^{-19}$ J. The finite element simulations are carried out with $d_c=2$ μm, $D_0=7.82$ μm, $\mu_h/\mu_0=1/20$, $\mu_0=5$, 8 and 12 μN/m, and $\kappa=2\times10^{-19}$ J.

Fig. 8 shows the CGMD simulation and finite element (FEM) simulations results of the increase in the axial diameter and the decrease in the transverse diameter of the RBC as a function of the force applied by the optical tweezers up to a maximum value of about 200 pN. The laser tweezers

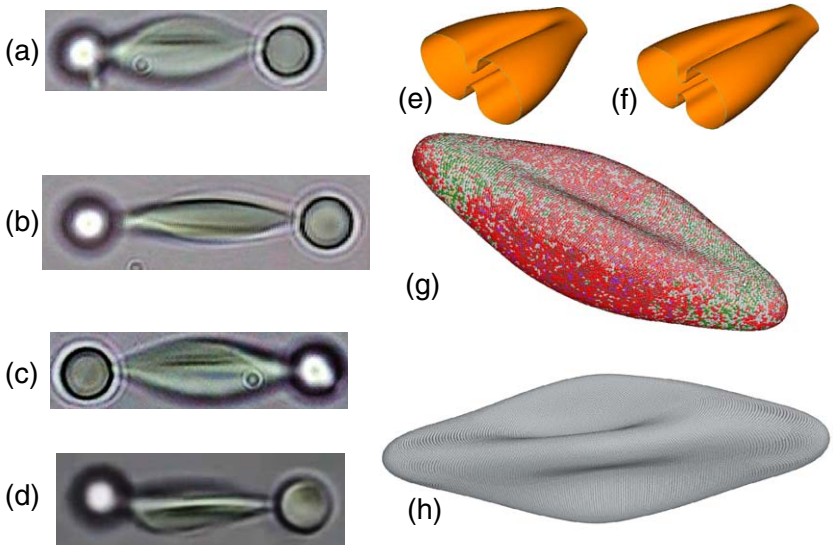

Fig. 9. Folding observed in experiments and computational simulations. (a)–(d) Optical tweezers experiments at stretching forces between 80–193 pN. (e) and (f) are FEM simulations based on continuum hyperelasticity [18] at forces of 67 and 193 pN, respectively. (g) and (h) are simulations based on spectrin level modeling at forces of 85 and 190 pN, respectively. See text for more details.

experimental results [18] are also plotted for comparison. It is clear from the simulations that, computational results using the shear modulus $\mu_0 \sim 8$ μN/m match well with the average experimental curve, while $\mu_0 = 5 \sim 12$ μN/m covers most of the experimental scatter.

3.3. Deformation induced folding during laser tweezers stretching

It was noted in finite element simulations as well as experiments that deformation induced folding were observed (see supplementary movies of simulations and experiments in our earlier work [9,17,18]). Fig. 9 summarizes different types of folding observed in experiments as well as in simulations. Fig. 9(a) shows a relatively deep folding along the center, while Fig. 9(b) is a more gradual folding. Fig. 9(c) and Fig. 9(d) show two cases of irregular T-shaped folding observed experimentally. Similarly, different degrees and types of folding are observed in the CGMD and FEM simulations. Fig. 9(e) and Fig. 9(f) show different degrees of folding along the center line in the FEM simulations. Fig. 9(g) shows a more gradual folding in the CGMD simulation shown in Fig. 8. Fig. 9(h) shows a T-shaped folding in the CGMD simulation with an initial cell geometry that is not symmetrically aligned with the axis of loading.

It is clear through simulation results as well as the experimental observations that the folded cell shape can be strongly influenced by the contact geometry of the beads (size and symmetry), the stretching force applied, the initial cell shape, and the bending and shear moduli of the RBC membrane.

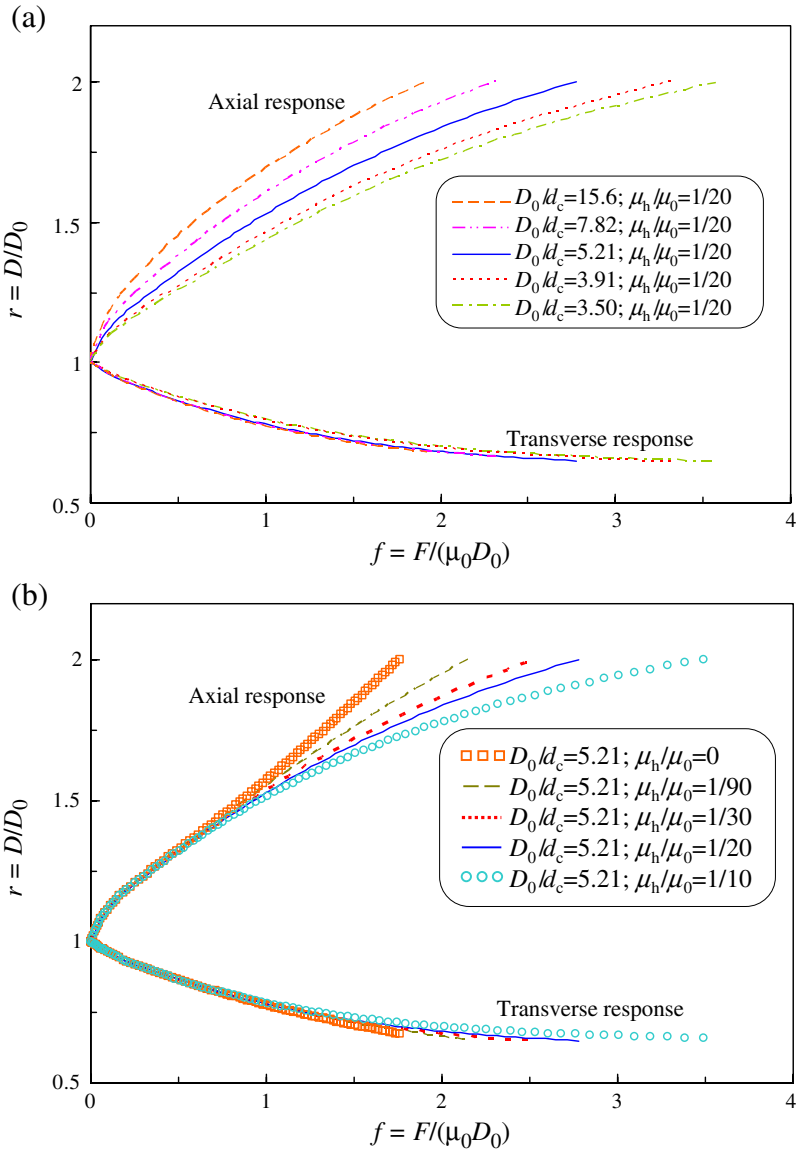

Fig. 10. Scaling relationships of RBC deformed by laser tweezers. (a) Dimensionless functions with a constant ratio of $\frac{\mu_h}{\mu_0} = \frac{1}{20}$, and (b) scaling functions with $\frac{D_0}{d_c} = 5.21$.

3.4. Scaling relationships and mechanical property extraction

Extracting mechanical properties from laser tweezers experiments is not a trivial task, because it requires complicated numerical simulations that can accurately describe the related geometrical parameters (i.e., cell size, shape, cytosol volume, and contact geometry) as well as the nonlinear constitutive parameters (i.e., shear and bending moduli). Establishing scaling relationships through dimensional analysis and parametric simulations, therefore, will provide insights of the inherent relationships between these various geometrical and constitutive parameters. A systematic methodology can also be established to accurately extract mechanical properties from a laser tweezers experiment, which will relieve the requirements of running a large number of sophisticated computational simulations.

For a laser tweezers experiment, the loading force F is a function of many different parameters:

$$F = F(D_A, \mu_0, \mu_h, \kappa, d_c, D_0, c_0, c_1, c_2) \tag{46}$$

Taking the cell shape factors c_0, c_1, c_2 as the standard values given above for the analytical biconcave shape, and noting that bending modulus κ within the experimentally observed range is not important for RBCs during large deformation stretching [17], we can simplify Eq. (46) to be

$$F = F(D_A, \mu_0, \mu_h, d_c, D_0) \tag{47}$$

Using the dimensional analysis and Π-theorem, Eq. (47) can be expressed as

$$\frac{F}{\mu_0 D_0} = \Pi'\left(\frac{D_A}{D_0}, \frac{D_0}{d_c}, \frac{\mu_h}{\mu_0}\right), \tag{48a}$$

and equivalently,

$$\frac{D_A}{D_0} = \Pi\left(\frac{F}{\mu_0 D_0}, \frac{D_0}{d_c}, \frac{\mu_h}{\mu_0}\right) \tag{48b}$$

where Π′ and Π are dimensionless functions.

Extensive parametric simulations using FEM with different combinations of parameter sets (μ_0, μ_h, κ, d_c, D_0) confirm that, with the same $\frac{D_0}{d_c}$ and $\frac{\mu_h}{\mu_0}$ ratio, different parameter sets give practically the same normalized force ($f = \frac{F}{\mu_0 D_0}$) versus normalized cell stretch ratio ($r = \frac{D_A}{D_0}$) curves. Fig. 10(a) plots the so obtained *r-f* functions with $\frac{\mu_h}{\mu_0} = \frac{1}{20}$, and Fig. 10(b) plots the *r-f* functions with $\frac{D_0}{d_c} = 5.21$. Fig. 10(a) shows the functional dependence of the Π functions versus different $\frac{D_0}{d_c}$ ratios; significant changes are found for the axial response across the entire stretching range studied, whereas only small variations are found for the transverse response. This demonstrates the importance to accurately measure both the contact diameter and initial cell size. Fig. 10(b) shows the functional dependence of the Π functions versus different $\frac{\mu_h}{\mu_0}$ ratios; significant changes are found for the axial response at larger stretch ratios but not at small stretch ratios, whereas much smaller variations are found for the transverse response. This shows that the early portion of the data can be used to extract the linear shear modulus μ_0, while the data at larger stretch ratios can be used to extract the strain hardening behavior (i.e., μ_h) of the nonlinear elasticity. Here we give one set of such dimensionless functions in closed-form based on hundreds of FEM computations that fit well all the range of parameters simulated,

$$\frac{D_A}{D_0} = 1 + B\left\{\frac{F}{\mu_0 D_0}\right\}^C,$$

$$B = B_1 + B_2\left[\ln\left(\frac{D_0}{d_c} - B_3\right)\right],\ C = C_1 - C_2\left[\ln\left(\frac{D_0}{d_c} - C_3\right)\right],$$

$$B_1 = 0.42054,\ B_2 = 0.059016 - 0.01489195\left[\ln\left(\frac{\mu_h}{\mu_0}\right)\right],$$

$$B_3 = 3.247842 + 0.4191616\left[\ln\left(\frac{\mu_h}{\mu_0}\right)\right] + 0.0424185\left[\ln\left(\frac{\mu_h}{\mu_0}\right)\right]^2.$$

$$C_1 = 0.5998124 - 0.0574776\left[\ln\left(\frac{\mu_h}{\mu_0}\right)\right] - 0.00348081\left[\ln\left(\frac{\mu_h}{\mu_0}\right)\right]^2,$$

$$C_2 = 0.04985,$$

$$C_3 = -1.93967 - 2.090442\left[\ln\left(\frac{\mu_h}{\mu_0}\right)\right] - 0.2258287\left[\ln\left(\frac{\mu_h}{\mu_0}\right)\right]^2, \tag{49}$$

where the parameter ranges are $\frac{D_0}{d_c} \in [3.5, 15.64]$ and $\frac{\mu_h}{\mu_0} \in \left[\frac{1}{90}, \frac{1}{10}\right]$, and the fitting is within the range $\frac{D_A}{D_0} \in [1, 1.8]$.

Now with the closed-form dimensionless functions given by Eq. (49), a systematic methodology can be readily established

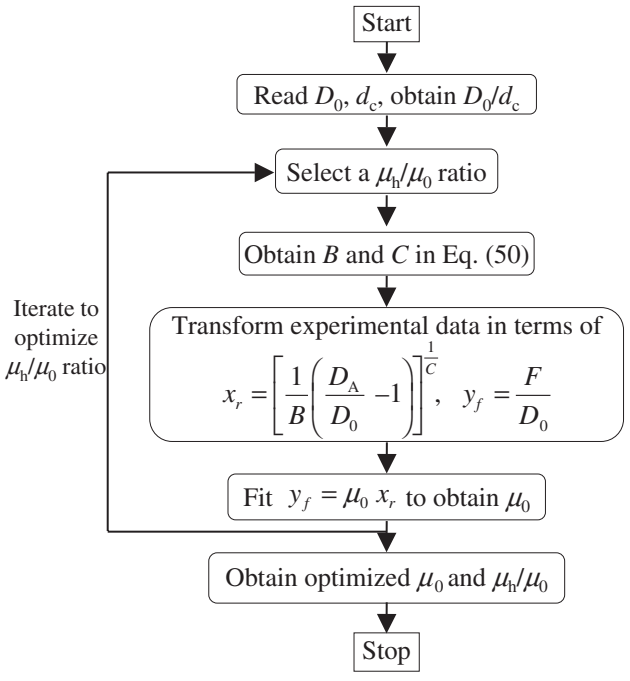

Fig. 11. Flow chart to extract elastic properties based on the proposed closed-form scaling functions.

Table 1
Illustrative examples of using the proposed scaling functions for extracting the elastic moduli of healthy and *P. falciparum*-invaded RBCs subjected to optical tweezers stretching

RBC condition	Method used*	Average μ_0 (μN/m)	Low error scatter value (μN/m)	High error scatter value (μN/m)	Number of tests
Healthy	Present scheme	8.5	6.1	10.9	7
	Ref. [9]	5.3	4.0	7.3	
Exposed	Present scheme	11.0	7.7	14.2	8
	Ref. [9]	8.0	6.0	10.7	
Ring	Present scheme	21.2	17.0	25.3	5
	Ref. [9]	16.0	12.6	21.3	
Trophozoite	Present scheme	40.0	22.6	57.5	5
	Ref. [9]	21.3	16.0	32.0	
Schizont	Present scheme	57.5	26.6	88.3	23
	Ref. [9]	53.3	33.0	100.0	

*Note: If the area conservation condition is strictly enforced, the μ_0 values extracted in this table need to be multiplied by a factor of 0.75 as discussed in Section 2.

as shown in Fig. 11. Various optimizing/fitting schemes other than the one shown in Fig. 11 can also be explored.

Using the proposed methodology, the experimental data reported earlier [9] are analyzed and compared with the results obtained by simply fitting the average experimental curve and the scatter. Table 1 shows the examples using this method for extracting the elastic moduli of healthy and *P. falciparum*-invaded RBCs that were subjected to large deformation by means of optical tweezers. For all cases studied in Table 1, we simply take $\mu_h/\mu_0=1/20$ for the purpose of extracting μ_0. The *P. falciparum*-invaded RBCs in schizont stage are more spherical than biconcave [9]. However, it was found that the axial responses are very close to each other for spherical and biconcave RBCs with the same membrane modulus as long as their initial diameters are the same [17]. Thus the issue of shape changes can be circumvented by simply using the current set of equations.

Comparing the results obtained using these two methods, it is clear that all the trends of shear modulus variation versus parasite development stages observed in Suresh et al. [9] are preserved, i.e., the shear modulus of RBC membrane increases up to 10-fold with progressive parasite development. In most cases the values obtained using these two methods are close to each other. In the case of trophozoite case, the average value estimated by the current scheme is considerably stiffer. This is due to the much smaller average $d_c=1.2$ μm for the trophozoite tests, while in Suresh et al. [9] it was simply assumed $d_c=2.0$ μm, which resulted in a lower estimate of the shear modulus.

4. Concluding remarks

In this work, we have provided explicit expressions for the membrane shear modulus μ_0, linear elastic area compression modulus K, and Young's modulus E for the human red blood cell with information derived from recent analytical, computational and experimental studies that employ force-displacement laws that conform to the worm-like chain model formulation. It is shown that the key parameters of the WLC model are consistent with the parameters extracted by matching whole cell, large deformation experiments with continuum models based on continuum, hyperelasticity formulations. The predictions of both spectrin-level and continuum values of elastic parameters of the composite membrane comprising the spectrin network are then compared with recent whole cell deformation experiments that employed optical tweezers stretching to large strain levels. Folding of the RBC membrane during deformation is observed both experimentally and computationally. From the spectrin-level and continuum-level computational simulations, it is clear that the folding is related to the irregular biconcave shape of the erythrocyte and that it is influenced by the constitutive response of the membrane and the spectrin network and by the conditions of contact where the glass beads are attached at diametrically opposite ends of the cell for the optical tweezers experiments. We also present closed-form scaling functions based on a large number of computations and dimensional analysis. This provides a systematic methodology to extract key mechanical parameters from optical tweezers experiments. Illustrative examples are given for the use of such methodology for extracting the elastic moduli of healthy and *P. falciparum*-invaded RBCs that were subjected to large deformation by means of optical tweezers.

Acknowledgments

This work was supported in part by the Singapore-MIT Alliance program on Molecular Engineering of Biological and Chemical Systems. The authors also acknowledge ongoing research collaborations between MIT and The Ohio State University on atomistic and molecular simulations of hard and soft materials which are supported by the Defense University Research Initiative on Nano Technology (DURINT) on ''Damage- and Failure-Resistant Nanostructured and Interfacial Materials'' by the Office of Naval Research under Grant N00014-01-1-0808.

References

[1] S. Eber, S.E. Lux, Seminars in Hematology 41 (2004) 118.
[2] P.G. Gallagher, Seminars in Hematology 41 (2004) 142.
[3] J. Delaunay, Seminars in Hematology 41 (2004) 165.
[4] C. Brugnara, Journal of Pediatric Hematology Oncology 25 (2003) 927.
[5] G. Bosman, Cellular and Molecular Biology 50 (2004) 81.
[6] O. Galkin, P.G. Vekilov, Journal of Molecular Biology 336 (2004) 43.
[7] B.M. Cooke, N. Mohandas, R.L. Coppell, Advances in Parasitology, vol. 50, Academic Press Ltd, London, 2001, p. 1.
[8] F.K. Glenister, R.L. Coppel, A.F. Cowman, N. Mohandas, B.M. Cooke, Blood 99 (2002) 1060.
[9] S. Suresh, J. Spatz, J.P. Mills, A. Micoulet, M. Dao, C.T. Lim, M. Beil, T. Seufferlein, Acta Biomaterialia 1 (2005) 15.
[10] E.A. Evans, R. Skalak, Mechanics and Thermodynamics of Biomembranes, CRC Press, Inc., Boca Raton, Florida, USA, 1980.

[11] Y.C. Fung, Biomechanics: Mechanical Properties Of Living Tissues, 2nd ed., Springer-Verlag, New York, USA, 1993.
[12] J.C. Hansen, R. Skalak, S. Chien, A. Hoger, Biophysical Journal 72 (1997) 2369.
[13] D.E. Discher, D.H. Boal, S.K. Boey, Biophysical Journal 75 (1998) 1584.
[14] N.S. Gov, S.A. Safran, Biophysical Journal 88 (2005) 1859.
[15] J. Li, M. Dao, C.T. Lim, S. Suresh, Biophysical Journal 88 (2005) 3707.
[16] C. Bustamante, Z. Bryant, S.B. Smith, Nature 421 (2003) 423.
[17] M. Dao, C.T. Lim, S. Suresh, Journal of the Mechanics and Physics of Solids 51 (2003) 2259 (also see Erratum ibid 53 (2005) 493–494).
[18] J.P. Mills, L. Qie, M. Dao, C.T. Lim, S. Suresh, Mechanics and Chemistry of Biosystems 1 (2004) 169.
[19] J.C. Winkelmann, B.G. Forget, Blood 81 (1993) 3173.
[20] D.E. Discher, D.H. Boal, S.K. Boey, Physical Review E 55 (1997) 4762.
[21] S.K. Boey, D.H. Boal, D.E. Discher, Biophysical Journal 75 (1998) 1573.
[22] J.C.M. Lee, D.T. Wong, D.E. Discher, Biophysical Journal 77 (1999) 853.
[23] W. Helfrich, Zeitschrift fur Naturforschung. C, A Journal of Biosciences 28 (1973) 693.
[24] D.H. Boal, Mechanics of the Cell, Cambridge University Press, Cambridge, U.K., 2002.
[25] R. Mukhopadhyay, G. Lim, M. Wortis, Biophysical Journal 82 (2002) 1756.
[26] J.F. Marko, E.D. Siggia, Macromolecules 28 (1995) 8759.
[27] M.P. Allen, D.J. Tildesley, Computer Simulation of Liquids, Clarendon Press, New York, 1987.
[28] J.C. Simo, K.S. Pister, Computer Methods in Applied Mechanics and Engineering 46 (1984) 201.
[29] O.H. Yeoh, Rubber Chemistry and Technology 63 (1990) 792.
[30] K.J. Van Vliet, J. Li, T. Zhu, S. Yip, S. Suresh, Physical Review B 67 (2003) (art. no.-104105).
[31] G. Lenormand, S. Henon, A. Richert, J. Simeon, F. Gallet, Biophysical Journal 81 (2001) 43.
[32] G. Bao, S. Suresh, Nature Materials 2 (2003) 715.
[33] E.A. Evans, Y.C. Fung, Microvascular Research 4 (1972) 335.